

EXPERIMENTAL STUDY OF GROUND EFFECT ON A HEAVING NACA0012 AEROFOIL

Mogeng Li[1], Michael A. Legovich[2] & Nicholas J. Lawson[1]

[1]School of Aerospace, Mechanical and Mechatronic Engineering, The University of Sydney, Darlington, NSW 2008, Australia

[2]Faculty of Engineering and Applied Science, Cranfield University, Cranfield, MK43 0AL, United Kingdom

Abstract

Unsteady aerodynamics in ground effect plays an important role in a wide range of engineering systems. For a stationary aerofoil, decreasing ground clearance leads to an initial increase in the normal force, followed by a reduction due to viscous effects. In this work, we specifically focus on the effect of ground proximity on dynamic stall. An experimental investigation of a heaving NACA0012 aerofoil operating in ground effect is conducted using stereoscopic particle image velocimetry and unsteady surface pressure measurements. Force hysteresis over an oscillation cycle is examined, and correlated with the measured velocity fields, providing insight into the interaction between the flow structures and the ground plane.

Keywords: unsteady aerodynamics; heaving aerofoil; ground effect; dynamic stall; particle image velocimetry

1. Introduction

Ground-effect unsteady aerodynamics is prevalent in many real-world applications. For example, the inverted front wing in Formula One racing plays a critical role in increasing vehicle downforce, enabling higher cornering speeds [1]. Wing-in-ground (WIG) vehicles exploit the aerodynamics benefit of increased lift and efficiency [2]. Similarly, many animals, including fish and birds, utilise ground effect to improve their propulsion efficiency [3, 4].

Ground effect studies can generally be classified into two categories based on aerofoil configuration. In the first category, the aerofoil is positioned above the ground in an upright position, generating a lift force that points away from the ground plane. This configuration is relevant to aircraft takeoff and landing, as well as WIG craft. In the second category, the aerofoil is placed in an inverted position, generating a downforce, with the front wing on a race car as a major application [5, 1]. Note that a symmetrical aerofoil at zero angle of attack also creates a suction between the aerofoil and ground plate [6], and is therefore included in this category. In both scenarios, ground effect is characterised by the ground clearance h_m (also known as ride height), which is the minimum distance between the aerofoil surface and the ground.

For a stationary aerofoil in ground effect, three main mechanisms affect its lift generation. The first is the straightening of streamlines near the ground, which reduces the effective angle of attack in both upright and inverted configurations [7], thereby reducing the generated lift and downforce. As the ground clearance decreases further, a second and more prominent mechanism prevails, which is non-circulatory in nature. For an inverted aerofoil, a diffuser forms between the aerofoil surface and the ground, and the resulting Venturi effect reduces pressure on the suction side of the aerofoil, enhancing downforce. For an upright aerofoil, on the other hand, the aerofoil surface and ground form a ‘nozzle’, which constraints the flow and locally increase the pressure on the pressure side of the aerofoil, leading to an increased lift [8]. Lastly, once the ground clearance falls below approximately 10% of wing chord, the normal force magnitude reduces again in both configurations and the benefit

of ground effect diminishes. For an inverted aerofoil, the reduction in downforce has been attributed to flow separation on the suction side [9, 10], or from the merging of the wake and the ground boundary layer [6]. For an upright aerofoil, separation of the ground boundary layer in addition to loss of suction on the aerofoil has been identified as the cause of lift reduction [11]. This regime has been termed 'extreme ground effect' by Moryossef and Levy [12], who suggested it occurs at ground clearances below approximately $0.5c$.

In parallel with the research on ground effect, unsteady aerodynamics, particularly aerofoils experiencing periodic oscillations, has received considerable attention [13, 14]. In such scenarios, flow unsteadiness is characterised by the reduced frequency, defined as $k = \pi f c / U_\infty$, where f is the oscillation frequency, c is the chord length of the aerofoil, and U_∞ is the freestream velocity. The analytical solution of an aerofoil oscillating with a small amplitude based on potential flow theory was first developed by Theodorsen [15], and later extended by Garrick [16] to account for drag and propulsive effects. In real fluids, however, the effect of viscosity leading to flow separation at parts of the cycle, causes significant deviation from inviscid predictions. Dynamic stall features a lift overshoot and a delay in the onset of massive flow separation with respect to static stall. Over a full oscillation cycle, the flow exhibits consecutive emergence and spreading of flow reversal on the aerofoil suction side, the formation and convection of a large-scale leading-edge vortex, massive flow separation, and flow reattachment [13, 14, 17].

The flow of a heaving aerofoil in ground effect is classified into three regimes based on the reduced frequency [10]: At low frequencies, the aerofoil can be treated as quasi-stationary and the ground effect governs the flow. The contribution of incidence effects becomes apparent at medium frequencies and can be explained by defining an effective angle of attack. The maximum downforce is obtained at high effective angles of attack. As the frequency is increased even further, the only apparent effect is that of added mass.

In this work, we focus on the regimes of low to medium reduced frequencies, with the aim of isolating the dynamic stall mechanisms in ground effect, particularly the interaction between dynamic stall flow structures and the ground.

2. Methods

2.1 Flow facility and heaving wing model

The experiments are conducted in the 4'×3' low-speed, closed-circuit wind tunnel at the University of Sydney. Figure 1(a) provides an overview of the experimental setup. A wing model with a NACA0012 profile is mounted vertically in the test section with its neutral position on the tunnel centreline. The full-span wing model has a chord length of $c = 0.3$ m. The aerofoil sections are 3D printed using polylactic acid (PLA) filaments and then bolted on a full-span aluminium spar. The outer surface

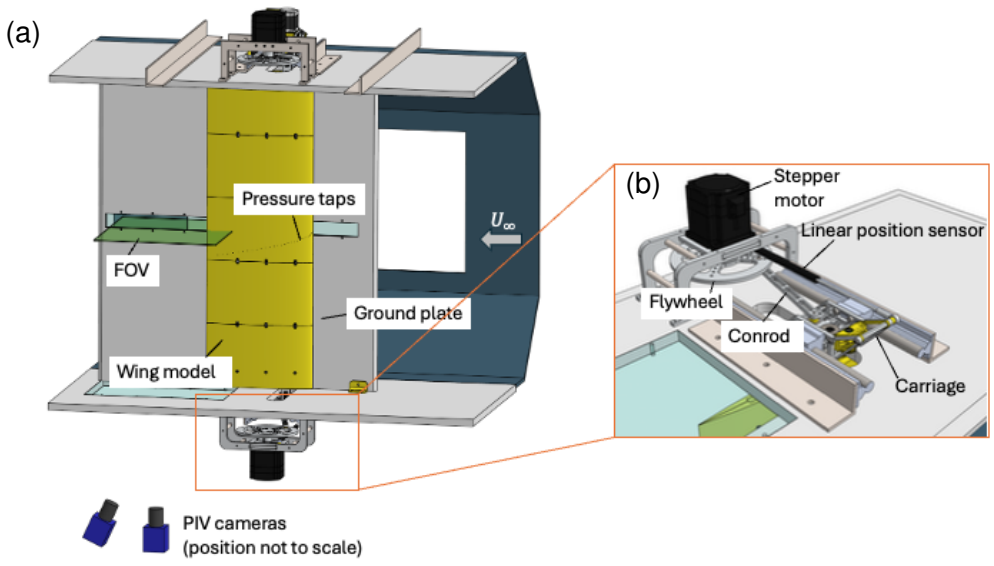


Figure 1 – (a) Experimental arrangement in the wind tunnel test section. (b) A magnified view of the heaving mechanism.

of the aerofoil sections is polished and spray painted matte black to reduce laser reflection. The quarter-chord point at the two ends of the aluminium spar are fixed to the carriages outside the wind tunnel, and the angle of attack of the model is set discretely using three different mounting fixtures (nominally $0°$, $10°$ and $-10°$). The heaving mechanisms on the top and bottom sides of the tunnel are the same: the carriage is mounted on a pair of linear guide rails, and connected through a conrod to a flywheel driven by a NEMA 34 stepper motor, as shown in Figure 1(b). The heaving amplitude H is determined by the radial position of the point on the flywheel to which the conrod is connected, and it is set to 45 mm $(0.15c)$ for all cases in the present work. The position of the wing is monitored by a Haltech HT-011203 linear position sensor mounted to the carriage. Control of the electronic system is enabled by an Arduino UNO R4. The accuracy of the aerofoil kinematic profile is validated using high-speed imaging, as detailed in the Appendix.

A ground plate is mounted at a fixed distance from the centreline, with its rounded leading edge located at 0.18 m upstream of the aerofoil leading edge. The boundary layer thickness on the ground plate at the leading edge of the aerofoil is estimated to be 2 mm. This configuration is selected, balancing the complexity of the experimental setup and ability to replicate the flow with a moving ground in the body-fixed reference frame. The ground clearance is varied by mounting the ground plate in different wall-normal locations, while the neutral position of the aerofoil remains the same. Different ground clearance cases are referred to by h_0/c, the normalised distance between the ground and the quarter-chord point when the aerofoil is at its neutral position. Another common method to characterise the ground clearance in the literature is to use the minimum gap between the aerofoil surface and the ground, denoted by h_m/c here. For the upright aerofoil, this occurs at the trailing edge, and for the neutral and inverted aerofoil, it falls near the thickest point of the aerofoil. The ground clearances of both definitions are summarised in Table 1.

case	$\alpha = 0°$				$\alpha = -10°$				$\alpha = 10°$	
x_m/c	0.3				0.1				1	
h_m/c (at $h/H = -1$)	∞	0.13	0.08	0.04	∞	0.12	0.07	0.03	∞	0.08
h_m/c (at $h/H = 0$)	∞	0.28	0.23	0.19	∞	0.27	0.22	0.18	∞	0.23
h_0/c	∞	0.34	0.29	0.25	∞	0.34	0.29	0.25	∞	0.34

Table 1 – Ground clearance of all cases, represented by h_0/c, quarter-chord height of the aerofoil at neutral position, and h_m/c, minimum gap between the aerofoil surface and the ground. x_m/c is the chord-wise location where the distance between the aerofoil surface and the ground is the smallest.

As shown in Figure 2, x represents the streamwise direction, and y represents the wall-normal direction, pointing away from the ground plate. The corresponding phase-averaged velocity components are U and V. The origin is placed at the nose of the aerofoil at $\alpha = 0°$ and neutral position (no heaving amplitude). All experiments are performed at a nominal freestream velocity of $U_\infty \approx 19$ ms^{-1}.The Reynolds number based on chord length is $Re \equiv U_\infty c/\nu = 3.9 \times 10^5$, where ν is the kinematic viscosity of air, and the reduced frequencies tested are $k = 0.05, 0.10$ and 0.15. The resulting maximum angles of attack due to the heaving motion of the aerofoil are $0.9°$, $1.7°$ and $2.6°$ for the three reduced frequencies, respectively, and they are reached when the aerofoil passes through the neutral position.

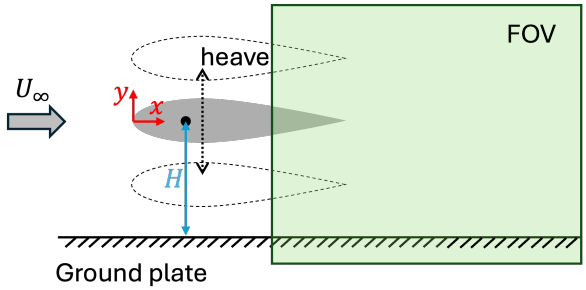


Figure 2 – Side view schematic of an aerofoil heaving near the ground plate, with coordinate system definition. The field-of-view captured by the PIV measurements is shown in green.

2.2 Surface pressure measurements

A total of 61 surface pressure taps are distributed around the mid-span of the wing model. The neighbouring pressure taps are placed 2.5 mm apart in the spanwise direction to avoid disturbances from upstream (see Figure 1a). The surface pressure tap inserts are connected to a MPS4264 Scanivalve (64 channels, 4" H_2O range) using vinyl tubes of about 1 m in length, with an inner diameter of 0.8 mm. The sampling frequency is 500 hz, and a minimum of 40 cycles per case are acquired and included in the phase averaging process. The time lag of the unsteady pressure signal is corrected using the rigid wall model described by Kutin and Svete [18].

2.3 Velocity field measurements

Stereoscopic PIV setup is selected to correct the perspective error [19]. A 532 nm double-pulsed laser beam is generated from an Nd:YAG laser (Litron Bernoulli 145-15 PIV), which is split into two with a beam splitter. The beams are then expanded into two light sheets, and sent into the test section from both front and back windows, enabling simultaneous measurement of both sides of the wing. DEHS particles with a diameter of $\lesssim 1$ μm are used as tracers. Two LaVision Imager CX-5 cameras (2448×2048 pixels, pixel size 2.740 μm) equipped with 16 mm lenses (C Series, Edmund Optics) are mounted under the tunnel test section, approximately 1 m from the laser sheet which is at the mid-span of the wing. The cameras subtend an angle of $19°$, and with $f_\# = 4.0$, no scheimpflug is required to achieve good focus across the image. The resulting field of view (FOV) is approximately 0.34×0.28 m^2 (equivalently $1.1 \times 0.9c^2$), as illustrated in Figure 2.

Synchronisation of the hardware is achieved by a Programmable Timing Unit (PTU). A PicoScope system (model: 6824E) generates a trigger signal based on the potential meter readings, which is sent to the PTU to realise phase-lock image acquisition. In each cycle, 20 equal-spaced phases are selected, and a total of 50 image pairs with $\Delta t = 80$μs (equivalent to a displacement of 10 pixels in the freestream) are acquired at each phase. Image acquisition and subsequent processing are both performed in DaVis 10. After background removal, the particle images are first processed with interrogation windows of 96×96 pixels with 50% overlap, followed by two passes of 32×32 pixels windows with 50% overlap. Median-filter-based universal outlier detection is applied to the resulting velocity field, and then the spurious vectors are replaced by interpolating neighbouring values.

3. Results

3.1 Aerodynamic coefficients and surface pressure distribution

3.1.1 Stationary aerofoil

We first report the time-averaged lift coefficient, C_l, of the aerofoil remaining stationary at $h = 0$, as shown in Figure 3. The measurements in the present work have a good agreement with the data in [20]. As the ground clearance h_0/c reduces from ∞ to 0.25 (equivalent to $h_m/c = 0.19$, see Table 1), the

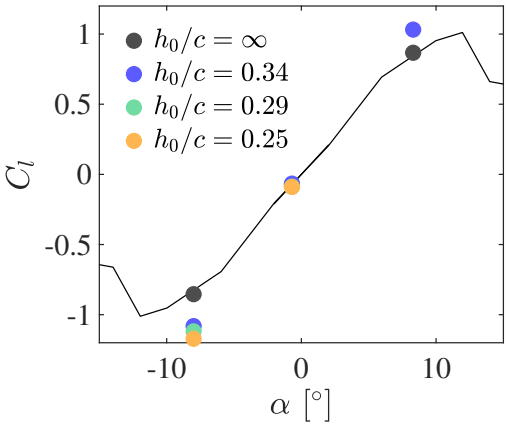


Figure 3 – Lift coefficient of a stationary aerofoil at the neutral position. Note that the angles of attack are determined from the PIV images, which deviate from the nominal value by approximately $1°$. The solid black line is the experimental data of a NACA 0012 aerofoil at a similar Reynolds number, $Re = 5 \times 10^5$ [20].

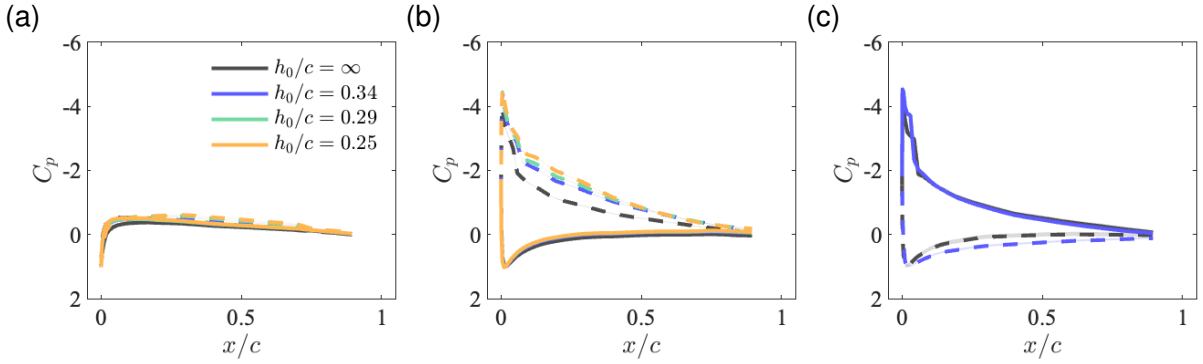


Figure 4 – Pressure coefficient C_p distribution of the stationary aerofoil at (a) $\alpha = 0°$, (b) $\alpha = -10°$, and (c) $\alpha = 10°$. Solid lines represent the upper surface (away from the ground), and dashed lines represent the lower surface (close to the ground). Shaded area is bounded by the 10- and 90-percentile of the data.

inverted aerofoil exhibits a stronger downforce, whereas the upright aerofoil shows an increase in the lift. The pressure distribution on the upper and lower sides of the aerofoil at $\alpha = 0°$ remains nearly identical (Figure 3a), as expected for a symmetrical geometry. For both inverted (Figure 4b) and upright (Figure 4c) aerofoil cases, pressure coefficient C_p reveals a strong suction peak of $C_p = -4.5$ near the leading edge, followed by a laminar separation bubble. As the ground clearance decreases, the main difference in the lift contribution between the upright and inverted aerofoils is from the lower surface (dashed lines). The inverted aerofoil experience a stronger suction on the lower side due to the Venturi effect, whereas the upright aerofoil sees an increase in the positive pressure. These observations are in line with the consensus of the literature [11, 8, 12].

3.1.2 Heaving aerofoil

The phase-averaged aerodynamic force and moment coefficients of the aerofoil heaving at a reduced frequency of $k = 0.1$ are shown in Figure 5. The theoretical solutions [15, 16] are also included in the figure for comparison. The theoretical solutions do not account for the effect of viscosity or the ground plate, but they compare well with the $h_0/c = \infty$ data, especially for the $\alpha = 0°$ case.

For the lift coefficients in Figure 5(a), the theoretical solution agrees with the measurements of the $h_0/c = \infty$ cases. At $\alpha = 0°$ (Figure 5a-i), for case $h_0/c = \infty$ where the ground plate is absent, the C_l trajectory is approximately centred about $C_l = 0$, and remains symmetrical on the $h > 0$ and $h < 0$ sides, as dictated by the symmetry of the wing kinematics and boundary conditions. In the upstroke, the relative motion of the aerofoil results in a negative effective angle of attack, the magnitude of which reaches its maximum $(1.7°)$ when the aerofoil passes through its neutral position. This leads to a slightly negative C_l on the upstroke branch, with the most negative C_l (minimum value) achieved near $h = 0$. In the presence of a ground plate, as h_0/c reduces, C_l becomes more negative at $h < 0$, indicating enhanced downforce generation due to ground effect. The lift coefficient exhibits a more complex behaviour for the inverted aerofoil, as shown in Figure 5(a-ii). For $h_0/c = \infty$, the C_l trajectory centres about $C_l = -0.8$ which is close to the static lift, but remains symmetrical otherwise. As h_0/c reduces to 0.34 and 0.29, a higher downforce (more negative C_l) is observed when the aerofoil is close to the ground, and the downforce is stronger in the downstroke compared to the upstroke, creating an inverted loop in the C_l trajectory. At $h_0/c = 0.25$, the smallest ground clearance tested, the highest downforce appears at $h/H = -0.5$ in the downstroke, and it oscillates as the aerofoil further approaches the ground plate. On the other hand, as the aerofoil departs from the ground in the upstroke, another local minimum C_l is achieved at $h/H = -0.8$, followed by lesser ones at $h/H = -0.1$, 0.09 and 0.6, creating a pattern with multiple undulations in a cycle. We speculate that this unusual behaviour may be caused by the structural vibration (aeroelasticity) when the ground clearance is very low, or the choking and subsequent restarting of the flow (the minimum gap between the aerofoil and the ground is only $0.03c$ at the aerofoil's lowest position). Further measurements are required to confirm this. For upright aerofoil with $\alpha = 10°$, the two smaller ground clearances were not tested due to geometric infeasibility. As shown in Figure 5(a-iii), the only ground effect case was with $h_0/c = 0.34$.

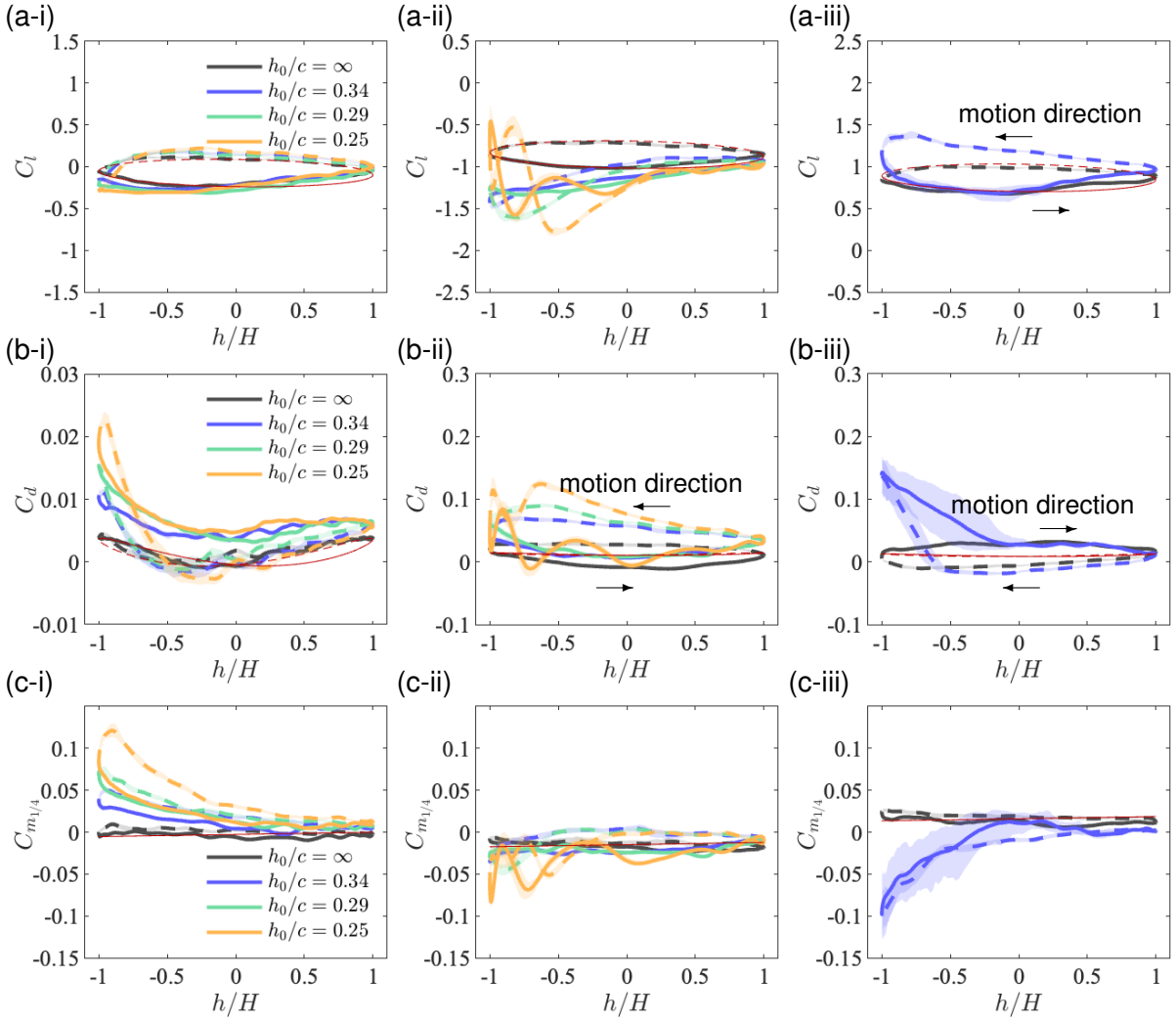


Figure 5 – Phase-averaged (a) lift coefficient, (b) drag coefficient, and (c) quarter-chord moment coefficient at $k = 0.1$. Left, middle, and right columns correspond to $\alpha = 0°$, $-10°$, and $10°$, respectively. The thin dark red line represents inviscid theory [15, 16] calculation of the $h_0/c = \infty$ case, with the corresponding static values superimposed. Solid lines represent upstroke, and dashed lines represent downstroke. Shaded area is bounded by the 10- and 90- percentile of the data at each phase from all cycles. Note that plot (b-i) has a different vertical axis range compared to (b-ii) and (b-iii), showing a magnified view of the drag coefficient at $\alpha = 0°$.

Compared to the $h_0/c = \infty$ case, a higher lift is generated in the downstroke, contributing to enhanced hysteresis.

The drag coefficient C_d calculated from surface pressure integral is shown in Figure 5(b). Note that the drag coefficients reported here underestimates the profile drag, because the frictional force contribution is not measured. First, the $h_0/c = \infty$ case with $\alpha = 0°$ compares favourably with the inviscid theoretical solution [16]. Without the added static drag, the inviscid theory predicts a positive averaged propulsive force (negative drag), but the magnitude is much smaller than the static pressure drag, so overall the heaving aerofoil exhibits drag rather than propulsive force. For the $\alpha = -10°$ and $10°$ cases, the inviscid theory does not capture the behaviour at $h_0/c = \infty$. The variation of C_d within a cycle is much greater than the prediction, and it follows a counterclockwise ($\alpha = -10°$) and clockwise ($\alpha = 10°$) trajectory, instead of the figure 8 pattern as predicted. In both cases, C_d is the highest when the effective angle is closest to 0, which corresponds to the downstroke for $\alpha = -10°$ and upstroke for $\alpha = 10°$. This observation signifies that at such reduced frequencies and Reynolds numbers, the measured pressure drag variation is strongly influenced by viscous effects, which cannot be captured by the inviscid theory. In the presence of the ground, the drag coefficient increases in all three angles (especially in the lower portion of the cycle). The $\alpha = 10°$ case shows the highest additional drag

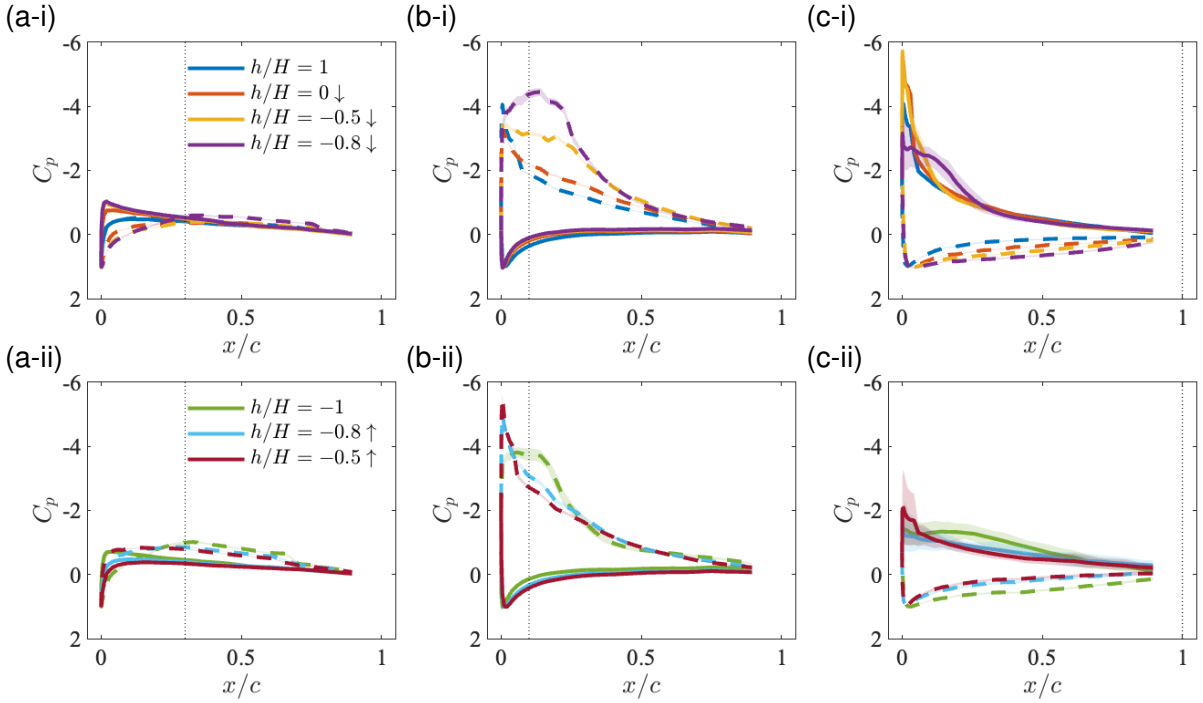


Figure 6 – Pressure coefficient C_p distribution of the heaving aerofoil at $k = 0.1$. (a) $\alpha = 0°$, $h_0/c = 0.29$, (b) $\alpha = -10°$, $h_0/c = 0.29$, and (c) $\alpha = 10°$, $h_0/c = 0.34$. Data from selected locations in the downstrokes and upstrokes are separated into top and bottom rows for clarity. Solid lines represent the upper surface (farther away from the ground), and dashed lines represent the lower surface (close to the ground). Shaded area is bounded by the 10- and 90- percentile of the data at each phase from all cycles. Vertical dashes line marks the location where the distance between the aerofoil lower surface and the ground plane is the smallest.

near ground, due to the flow separation on the aerofoil. However, compared to the ground-free case, the drag has a slight reduction (more negative drag) at $h/H > -0.5$ in the downstroke until the onset of flow separation.

Finally, in terms of quarter-chord moment coefficient $C_{m_{1/4}}$ in Figure 5(c), without a ground, the heaving motion does not have much influence on $C_{m_{1/4}}$. The ground plate leads to a negative (nose-down) $C_{m_{1/4}}$ at $\alpha = -10°$ and $10°$, but a positive (nose-up) $C_{m_{1/4}}$ at $\alpha = 0°$. This will be further discussed in connection with the pressure distribution in Figure 6 later in this section.

The pressure coefficient C_p of the heaving aerofoil at a number of phases near the ground are summarised in Figure 6. For all three cases included here for comparison, the ground clearance is selected such that the minimum clearance at $h/H = -1$ is approximately 0.08 (see Table 1). Similar to the stationary results in Figure 4, the main difference in the pressure distribution with decreasing ground clearance is on the lower side (dashed lines). For $\alpha = 0°$ in Figure 6(a), the suction increases in a broad region near $x/c = 0.3$, which is the throat of the Venturi nozzle formed between the aerofoil surface and the ground. For $\alpha = -10°$ in Figure 6(b), maximum suction appears at $x/c = 0.1$, also corresponding to the location of the narrowest region of fluid passage. Comparing Figure 6(a) and (b), although the nozzle throat has similar sizes, the local velocity entering the nozzle is much faster in the latter due to the flow acceleration over the strong suction peak ($C_p \approx -4$ compared to $C_p \approx -1$ in Figure 6a), resulting in a more prominent enhancement of the downforce in the $\alpha = -10°$ case. The difference in the nozzle throat location between these two cases also explains the change of sign in $C_{m_{1/4}}$ (Figure 5c). For $\alpha = 0°$, ground proximity leads to a stronger suction (negative) pressure around $x/c = 0.3$ on the lower side, and this additional downforce applied aft the quarter-chord point results in a positive $C_{m_{1/4}}$. For $\alpha = -10°$ on the other hand, the increase of suction pressure occurs near $x/c = 0.1$, which is before the quarter-chord point, and it generates a negative $C_{m_{1/4}}$. These observations highlights that in the design of inverted aerofoils operating near ground, location of the Venturi nozzle throat can influence the moment coefficient. If the design goal is to avoid introducing

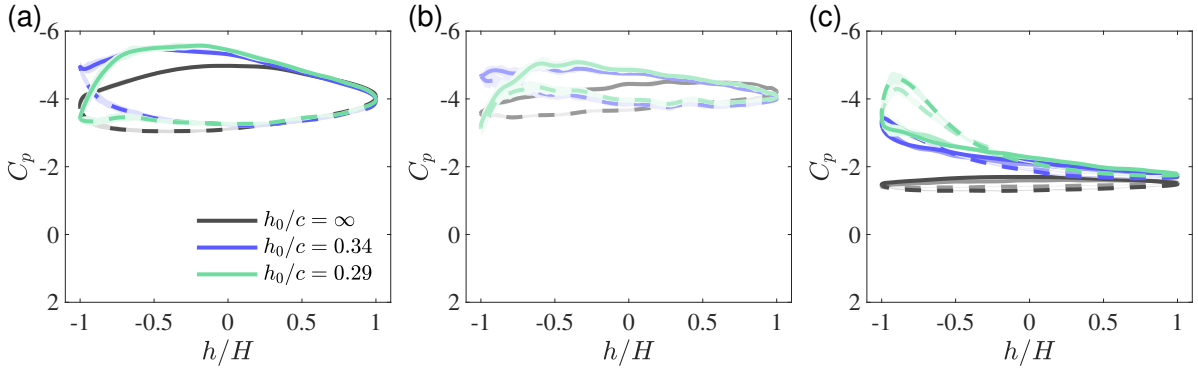


Figure 7 – Pressure coefficient C_p of the $\alpha = -10^\circ$ cases in a heaving cycle. (a) $k = 0.1$, $x/c = 0.005$; (b) $k = 0.05$, $x/c = 0.005$; (c) $k = 0.05$ and 0.1, $x/c = 0.1$. The lighter shaded lines represent data at a lower reduced frequency of $k = 0.05$. Dashed lines represent downstrokes and solid lines represent upstrokes.

additional pitching motion of the aerofoil near the ground, then it is desirable to select an aerofoil angle such that the Venturi nozzle throat is close to the quarter-chord point.

Next, we examine the cyclic variation of the pressure at two monitor points. The first monitor point is at $x/c = 0.005$ on the lower side of the aerofoil, which captures the suction peak. The peak strength varies within the cycle, and the magnitude also decreases approximately proportionally, with k reduces from 0.1 to 0.05 (Figure 7a and b). This indicates that the suction peak is primarily dependent on the effective angle of attack due to aerofoil motion, with some minor influence of the ground especially in the lower half of the cycle. The second monitor point (Figure 7c) is selected at $x/c = 0.1$ on the lower side, which is approximately the closest point on the aerofoil surface to the ground plane. The pressure at this point is primarily associated with Venturi effect, which is determined by the ground clearance with little hysteresis when the nozzle throat is larger than $0.23c$. When the nozzle throat reduces below $0.23c$, the suction enhancement increases at a higher rate in the downstroke, forming a hysteresis loop. In other words, the aerofoil generates a stronger suction at the nozzle throat in the 'cleaner' flow in the downstroke, but this enhancement diminishes when the aerofoil enters the upstroke. The dependence on k is small in most part of the cycle. These observations compare favourably with the static results of [8], where compared to the leading-edge suction peak, the negative pressure associated with the Venturi effect strengthens more significantly with reducing ground clearance.

Finally, for $\alpha = 10^\circ$ in Figure 6(c), the positive pressure on the lower side of the aerofoil (which is facing the ground plane) increases with decreasing distance from the ground, similar to the observations in static ground effect [8]. On the upper (suction) side, the suction peak diminishes as the aerofoil approaches the ground in the downstroke, indicating a leading-edge separation on the upper side. The static ground effect study of [11] reported a loss of lift at small ground clearances due to both trailing-edge separation of the aerofoil, and reduced positive pressure on the lower side of the aerofoil due to ground boundary layer separation.

3.2 Velocity fields

Selected phased-averaged streamwise velocity contours of the three aerofoil angles are summarised in Figures 8–10.

For the $\alpha = -10^\circ$ case, without a ground plate, as shown in Figure 8(a), the aerofoil's wake remains narrow, and the suction increases as the aerofoil accelerates upwards. For case $h_0/c = 0.34$ in Figure 8(b), boundary layer on the ground plate thickens between $h/H = -1.00$ and $h/H = -0.57\uparrow$ (when the aerofoil is moving away from the ground from its lowest heaving position), but no flow separation is observed. When the ground clearance is reduced to $h_0/c = 0.29$, there is strong interaction between the ground boundary layer and the aerofoil wake. The aerofoil wake deflects downwards and merges with the ground boundary layer, as evidenced by the low-speed regions in the second and third panels of Figure 8(c). In these two cases, the pressure distribution (and thus C_l) behaves similarly in the upstroke. However, as the aerofoil approaches the ground, there is a shift from aerofoil suction

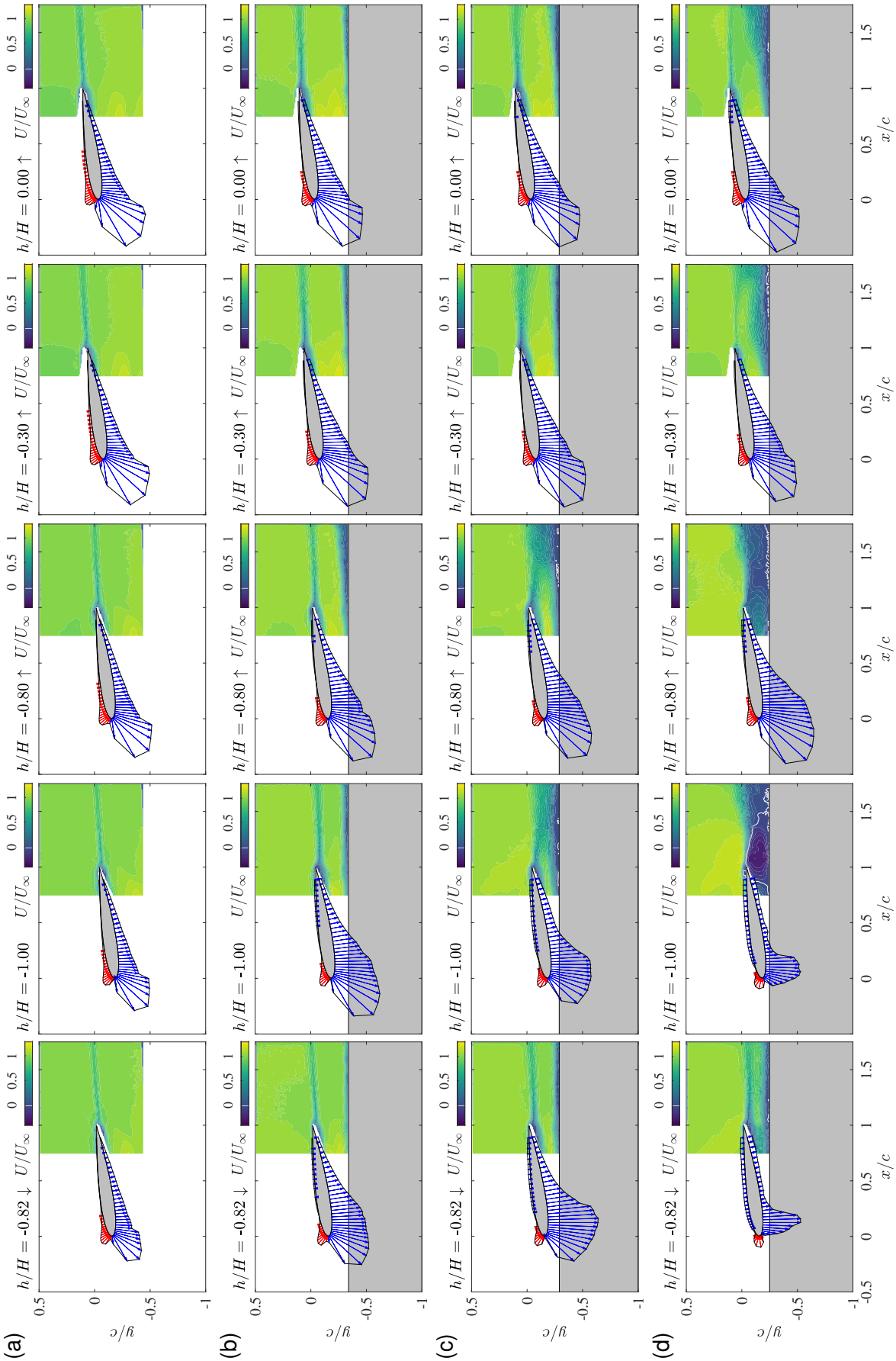


Figure 8 – Phase-averaged streamwise velocity fields at $k = 0.1$, $\alpha = -10°$, (a) $h_0/c = \infty$, (b) $h_0/c = 0.34$, (c) $h_0/c = 0.29$, and (d) $h_0/c = 0.25$. The phase-averaged pressure distribution is also included as vectors around the aerofoil, with red and blue colours representing positive and negative pressures, respectively.

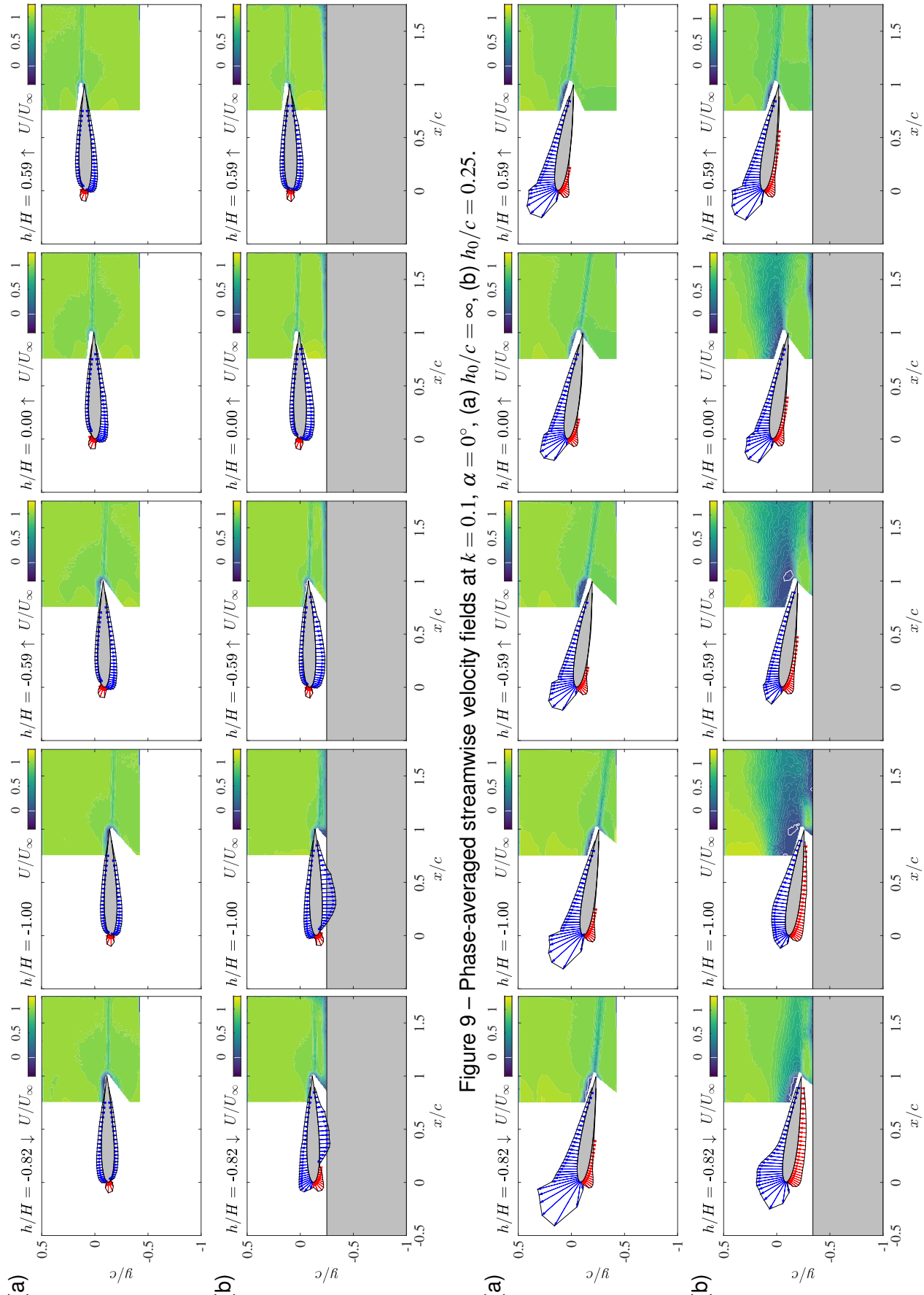


Figure 9 – Phase-averaged streamwise velocity fields at $k = 0.1$, $\alpha = 0°$, (a) $h_0/c = \infty$, (b) $h_0/c = 0.25$.

Figure 10 – Phase-averaged streamwise velocity fields at $k = 0.1$, $\alpha = 10°$, (a) $h_0/c = \infty$, (b) $h_0/c = 0.34$.

peak (close to the leading edge) to the Venturi effect (peak at $x/c \approx 0.1$) as the main contributor of the downforce. At $h_0/c = 0.25$ (Figure 8d), the smallest ground clearance tested, a large region of reversed flow appears downstream of aerofoil at $h/H = -1$ (second panel), possibly as a result of the flow being choked at the very narrow nozzle throat ($0.03c$). The separated flow recovers and the suction peak near the leading edge reestablishes in the subsequent phases, while the ground boundary layer still remains thickened, as a result of the adverse pressure gradient.

The velocity fields of the $\alpha = 0^\circ$ aerofoil at $h_0/c = \infty$ and 0.25 are shown in Figure 9. In both ground-free and ground-present cases, the wake remains narrow, indicating attached flow. At the aerofoil's lowest position $h/H = -1$, the wake thickens slightly in the ground effect case, but there is little evidence of its merge with the ground boundary layer.

For the upright aerofoil, the most distinct feature is the flow separation on the upper side and loss of the suction peak, as shown in Figure 10(b). This observation supports the pressure (Figure 6c) and force (Figure 5a-iii and b-iii) results. In comparison, the flow is attached and the aerofoil wake remains narrow throughout in the ground-free case. In the $h_0/c = 0.34$ case, flow separation initiates at $h/H = -0.82\downarrow$, slowing down the increase of C_l with reducing ground distance (see Figure 5a-iii). The separated flow persists for more than a quarter of a cycle, until a narrow wake re-establishes at $h/H = 0.59\uparrow$, and the suction peak similar to that in the $h_0/c = \infty$ case reappears. The beginning and end of the separated flow correspond well with the heaving positions where C_d exceeds the ground-free values (Figure 5b-iii).

4. Conclusions

In this study, we experimentally investigate the surface pressure distribution and velocity fields of a heaving aerofoil in ground effect. Special attention is given to separating flows, which were less covered in previous works.

For the inverted aerofoil, ground proximity leads to increased downforce and drag forces, and the deviation from the ground-free case appears when the aerofoil approaches the ground in the downstroke, and recovers when the aerofoil heaves away from the ground in the upstroke. The wall-normal location of the onset of ground effect is lower than that of the recovery (i.e. the aerodynamic effect due to ground lags the heaving position variation), which is mainly contributed by the variation of the suction peak strength. The suction pressure at the throat of the Venturi nozzle formed between the aerofoil and the ground contributes to the enhanced downforce near ground, especially in the downstroke. Interaction between the aerofoil wake and the ground boundary layer, as well as flow separation, are observed in the $h_0/c = 0.29$ and $h_0/c = 0.25$ cases. The flow separation is considered to be initiated by the choking of the flow at the narrow gap formed between the aerofoil and the ground. For the upright aerofoil, the ground plane increases the positive pressure on the lower side of the aerofoil, especially in the downstroke. On the upper side, the ground initially strengthens the suction peak, but triggers a leading edge separation in the lower half of the downstroke, leading to a reduction in the total lift.

In summary, this work characterises the aerodynamic forces and flow field of an aerofoil heaving in extreme ground effect, with a focus on flow separation. Effects of the reduced frequency and ground clearance on the lift/downforce enhancement mechanisms are discussed. Numerical simulations at matched flow conditions, as well as PIV measurements of the velocity field between the aerofoil and the ground will provide more detailed information on the flow behaviour in the gap region.

Acknowledgement

The authors would like to thank Devansh Prathap Kakkar for his assistance in the preparation of the PIV setup, and Zac Wilkins for his preliminary work in developing the aerofoil oscillation mechanism. The technical support from TSS workshop at the University of Sydney, in particular Kan Ye, Maohua Li, Hongjian Wang, and Philip Thompson, is gratefully acknowledged.

Appendix: Positioning accuracy of the heaving mechanism

The motion of the heaving aerofoil is characterised by high-speed imaging (Phantom MIRO LAB110, 1280×800 pixels resolution, sampled at 200 Hz) in the xy-plane, with some example images shown in Figure 11(a). The position of the aerofoil trailing edge is extracted through an image cross-correlation

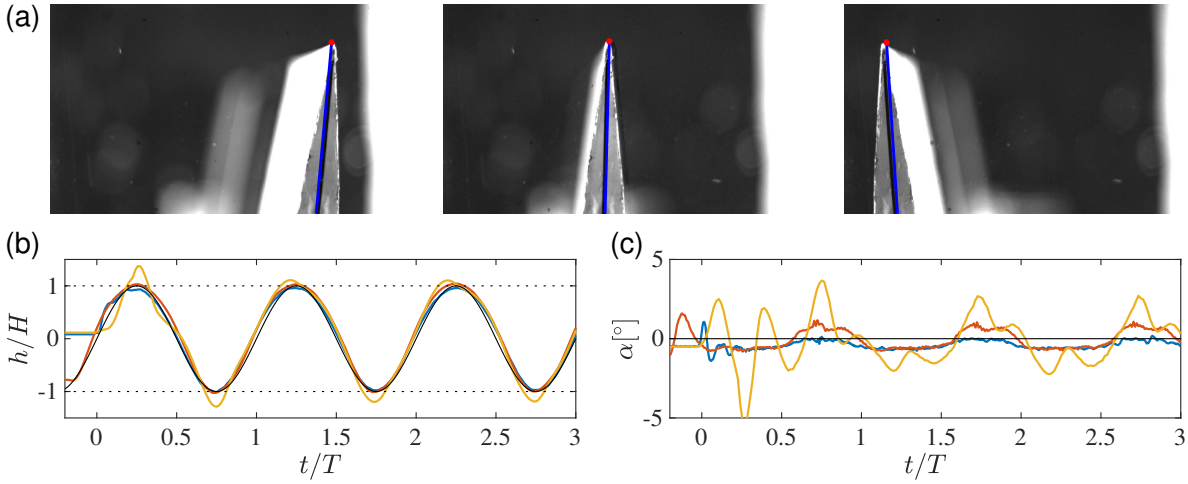


Figure 11 – (a) Sample images of the wing at various phases; (b) heaving position and (c) angle of attack of the first three cycles. Blue, red, and yellow colours correspond to $k = 0.05$, 0.1, and 0.15.

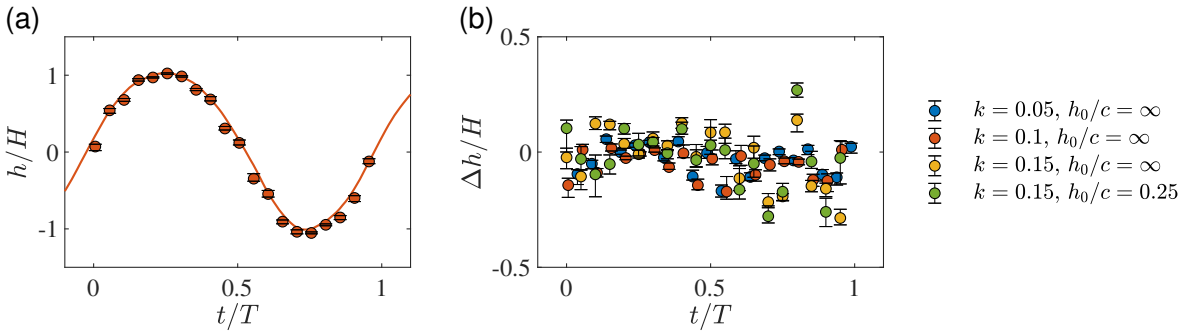


Figure 12 – (a) Averaged trailing edge location in each PIV acquisition phase (symbols), compared to the heaving position measured by high-speed imaging (solid line). (b) Difference between the phase-locked PIV images and corresponding heaving position measured by high-speed imaging. Error bars in both plots represent the minimum and maximum values acquired in each phase.

algorithm, and the angle of the aerofoil is found by detecting the chord line printed on the cross-section of the aerofoil. Figure 11(b) and (c) compares the heaving position and angles of the aerofoil at three reduced frequencies. In all cases, the first oscillation cycle after the start of the motion exhibit larges deviation from the prescribed motion profile (sinusoidal heaving position and zero pitch angle), but the motion stabilises in subsequent cycles with good repeatability. In the two lower frequency cases, $k = 0.05$ and 0.1, the heaving position remains close to the sinusoidal profile, and the pitch angle deviation is less than $1°$. In the $k = 0.15$ case, however, the trailing edge position overshoots by approximately 15% of the heaving amplitude at the maximum and minimum locations, and the pitch angle deviation is approximately $\pm 2.5°$. This more substantial deviation from the prescribed motion profile is due to the insufficient fitting tolerance of the heaving mechanism.

The trigger accuracy and jittering in the phase-locked PIV images is further examined by extracting the trailing edge locations, and the results are presented in Figure 12. The difference between the phase-locked PIV images and corresponding heaving position measured by high-speed imaging, Δh, represents the timing accuracy of the trigger signal, and it is smaller than $0.15H$ for most cases. The scatter of the trailing edge position within each phase, as characterised by the error bars, remains within $\pm 0.03H$ for most cases, evidencing a very low level of jittering. There is also no systematic difference between the $h_0/c = \infty$ and $h_0/c = 0.25$ cases, indicating that the model does not deflect significantly in the presence of the ground plate.

In summary, the current heaving mechanism is capable of achieving accurate sinusoidal motion profile with good repeatability after the first cycle from starting position. The phase-lock triggering has high repeatability between cycles. Therefore, in the paper, we focus more on the $k = 0.05$ and 0.1 cases, and treat the $k = 0.15$ cases with caution, due to the deviation of their motion profile from the input.

Copyright Statement

The authors confirm that they, and/or their company or organization, hold copyright on all of the original material included in this paper. The authors also confirm that they have obtained permission, from the copyright holder of any third party material included in this paper, to publish it as part of their paper. The authors confirm that they give permission, or have obtained permission from the copyright holder of this paper, for the publication and distribution of this paper as part of the ICAS proceedings or as individual off-prints from the proceedings.

References

[1] J. Katz. Aerodynamics of race cars. *Annu. Rev. Fluid Mech.*, 38(1):27–63, 2006.

[2] K. V. Rozhdestvensky. Wing-in-ground effect vehicles. *Prog. Aerosp. Sci.*, 42(3):211–283, 2006.

[3] A. Mivehchi, Q. Zhong, M. Kurt, D. B. Quinn, and K. W. Moored. Scaling laws for the propulsive performance of a purely pitching foil in ground effect. *J. Fluid Mech.*, 919:R1, 2021.

[4] K. Zheng, S. He, X. Zhao, L. Shen, and X. Zhu. Free-surface-induced ground effect for flapping swimmers. *J. Fluid Mech.*, 997:A36, 2024.

[5] R. G. Dominy. Aerodynamics of Grand Prix cars. *Proceedings of the Institution of Mechanical Engineers, Part D: Journal of Automobile Engineering*, 206(4):267–274, 1992.

[6] R. Ranzenbach and J. B. Barlow. Two-dimensional airfoil in ground effect, an experimental and computational study. Technical report, SAE Technical Paper, 1994.

[7] C. Coulliette and A. Plotkin. Aerofoil ground effect revisited. *Aeronaut. J.*, 100(992):65–74, 1996.

[8] J. W. Vogt and T. J. Barber. Ground effect phenomena about lift and downforce generating cambered aerofoils. *Int. J. Numer. Methods Heat Fluid Flow*, 22(2):153–174, 2012.

[9] J. Zerihan and X. Zhang. Aerodynamics of a single element wing in ground effect. *J. Aircraft*, 37(6):1058–1064, 2000.

[10] J. Molina and X. Zhang. Aerodynamics of a heaving airfoil in ground effect. *AIAA J.*, 49(6):1168–1179, 2011.

[11] C.-M. Hsiun and C.-K. Chen. Aerodynamic characteristics of a two-dimensional airfoil with ground effect. *J. Aircraft*, 33(2):386–392, 1996.

[12] Y. Moryossef and Y. Levy. Effect of oscillations on airfoils in close proximity to the ground. *AIAA J.*, 42(9):1755–1764, 2004.

[13] W. J. McCroskey. Unsteady airfoils. *Annu. Rev. of Fluid Mech.*, 14(1):285–311, 1982.

[14] L. W. Carr. Progress in analysis and prediction of dynamic stall. *J. Aircraft*, 25(1):6–17, 1988.

[15] T. Theodorsen. General theory of aerodynamic instability and the mechanism of flutter. Technical report, National Advisory Committee for Aeronautics, Langley, 1935. NACA-TR-496.

[16] I. E. Garrick. Propulsion of a flapping and oscillating airfoil. Technical report, National Advisory Committee for Aeronautics, Langley, 1936. NACA-TR-567.

[17] K. Mulleners and M. Raffel. The onset of dynamic stall revisited. *Exp. Fluids*, 52(3):779–793, 2012.

[18] J. Kutin and A. Svete. On the theory of the frequency response of gas and liquid pressure measurement systems with connecting tubes. *Meas. Sci. Technol.*, 29(12):125108, 2018.

[19] M. Reeves and N. J. Lawson. Evaluation and correction of perspective errors in endoscopic PIV. *Exp. Fluids*, 36(5):701–705, 2004.

[20] C. C. Critzos, H. H. Heyson, and R. W. Boswinkle. Aerodynamic characteristics of NACA 0012 airfoil section at angles of attack from 0° to 180°. Technical report, National Advisory Committee for Aeronautics, 1955.